Three-dimensional simulations of void collapse in energetic materials

Nirmal Kumar Rai* and H. S. Udaykumar†
Department of Mechanical and Industrial Engineering, The University of Iowa, Iowa City, Iowa 52242, USA

(Received 12 October 2017; published 6 March 2018)

The collapse of voids in porous energetic materials leads to hot-spot formation and reaction initiation. This work advances the current knowledge of the dynamics of void collapse and hot-spot formation using 3D reactive void collapse simulations in HMX. Four different void shapes, i.e., sphere, cylinder, plate, and ellipsoid, are studied. For all four shapes, collapse generates complex three-dimensional (3D) baroclinic vortical structures. The hot spots are collocated with regions of intense vorticity. The differences in the vortical structures for the different void shapes are shown to significantly impact the relative sensitivity of the voids. Voids of high surface area generate hot spots of greater intensity; intricate, highly contorted vortical structures lead to hot spots of corresponding tortuosity and therefore enhanced growth rates of reaction fronts. In addition, all 3D voids are shown to be more sensitive than their two-dimensional (2D) counterparts. The results provide physical insights into hot-spot formation and growth and point to the limitations of 2D analyses of hot-spot formation.

DOI: 10.1103/PhysRevFluids.3.033201

I. INTRODUCTION

Void collapse is an important mechanism for hot-spot formation and reaction initiation in heterogeneous energetic materials [1–4]. In real microstructures of energetic materials, voids of arbitrary shapes and orientations are present. The sensitivity of voids to imposed loads and therefore the formation of hot spots is strongly dependent on void morphology [5–8]. This work studies the collapse behavior of voids of various shapes commonly present in the microstructures of energetic materials by performing three-dimensional (3D) reactive void collapse simulations in otherwise uniform, isotropic HMX. The simulations provide important insights into the dynamics of void collapse-induced hot-spot formation and its dependence on void shapes. In particular, the limitations of two-dimensional (2D) simulations of hot-spot formation are quantitatively assessed by comparing the sensitivity of 3D void shapes to their 2D counterparts.

Previous 2D void collapse studies [2,5,6,8–14] provide insight into the mechanism of void collapse. For instance, in the hydrodynamic regime material jetting is a dominant collapse mechanism for circular voids [6,7,11,14,15]. On the other hand, the collapse of elongated void involves repeated pinching of void surfaces [8]. For both circular and noncircular voids, the collapse event involves generation of high-intensity baroclinic vorticity fields [8,14], and the cores of the vortices are the sites for maximum reaction progression and temperature rise. The generation of the high-intensity vorticity field is therefore connected with the sensitivity of the voids. However, this understanding is based on 2D analysis. In 3D, the generation of baroclinic vorticity field and subsequent instabilities are expected to be more pronounced and can have a significant effect on void sensitivity.

Two-dimensional mesoscale simulations show that sensitivity of voids is strongly dependent on void shapes [5–9]. Circular voids have been shown to be less sensitive than elongated voids in

*nirmalkumar-rai@uiowa.edu
†hs-kumar@uiowa.edu

both TATB-based [5] and HMX-based [8] energetic materials. In addition, for elongated voids, the sensitivity is significantly influenced by changes in orientations and aspect ratios [8]. Axisymmetric analysis of spherical and spheroidal (oblate and prolate) voids shows that oblate spheroids are more efficient in generating high-intensity hot spots [6]. Furthermore, conical and elliptical voids show higher sensitivity compared to spherical voids [7]. Therefore, 2D analysis provides evidence regarding the dependence of void sensitivity on its shape. However, the effect of void shape on sensitivity has not been studied in 3D except through 2D axisymmetric analysis. The axisymmetric modeling is only feasible for 3D voids exhibiting two planes of symmetry. It is not applicable for voids with arbitrary orientations and aspect ratios that are commonly present in the microstructure of energetic materials. Therefore, dependency of void sensitivity on void shape remains unexamined in 3D for general shapes and orientations.

The literature on the study of void collapse in 3D is not extensive. Among the few studies in this field, the analysis is performed for spherical voids only [12]; such studies compare the relative sensitivity of 3D and 2D void collapse through predictions of temperatures following inert void collapse. The 3D (spherical) void shows higher temperature rise and increased sensitivity than its 2D counterpart. The discrepancies between the prediction of 3D and 2D analysis can be even more significant for other void morphologies, such as platelike or rodlike voids. In this paper, the effect of void shape on the sensitivity is studied using four void shapes: sphere, cylinder, plate, and ellipsoid. For the different shaped voids, a comparative study between the sensitivity of 3D voids and the corresponding 2D counterparts is performed to understand the differences between the physics and void sensitivity measures that arise due to three-dimensionality. Since 3D computations of reactive shock dynamics of voids are more expensive than 2D computations, and parametric studies are likely to be predominantly 2D in the near future, the current work provides insights into the limits of 2D analysis of void collapse.

In this work, the mechanism of void collapse leading to hot-spot formation and reaction initiation is analyzed using 3D reactive void collapse simulation in an otherwise uniform HMX matrix under shock loading. A sharp Cartesian-based Eulerian framework [16–19] is used to perform the void collapse simulations. HMX chemical decomposition is modeled using Tarver's three-step reaction model [20]. The rest of the paper is organized as follows. Section II presents a brief outline of the governing equations and numerical framework used for the 3D analysis. In Sec. III A, the dynamics of void collapse and hot-spot formation is presented for all four void shapes. Following this, Sec. III B quantifies the sensitivity of the four void shapes. Section III C then compares the sensitivity prediction of 3D voids and their 2D counterparts. Finally, conclusions and further possible extensions of the work are discussed in Sec. IV.

II. METHODS

A sharp interface Cartesian grid-based Eulerian framework is used to perform 3D void collapse simulations. A detailed description of the numerical framework is presented in previous works [14,17]. Here, a brief description of the governing equations and material models is provided.

A. Governing equations

The governing equations are composed of hyperbolic conservation laws for mass, momentum, and energy:

$$\frac{\partial \rho}{\partial t} + \mathrm{div}(\rho \vec{V}) = 0, \tag{1}$$

$$\frac{\partial \rho \vec{V}}{\partial t} + \mathrm{div}(\rho \vec{V} \otimes \vec{V} - \sigma) = 0, \tag{2}$$

$$\frac{\partial \rho E}{\partial t} + \mathrm{div}(\rho E \vec{V} - \sigma \vec{V}) = 0, \tag{3}$$

where, $\vec{V}$ is velocity, ρ is density, E is the total specific energy (including internal and kinetic energy), and σ is the Cauchy stress tensor. The stress state of material σ can be decomposed into a deviatoric part S and dilatational part P:

$$\sigma = S - PI. \tag{4}$$

In the current Prandtl-Reuss formulation [21] the deviatoric stress tensor S is obtained by solving the evolution equation in the rate form:

$$\frac{\partial \rho S}{\partial t} + \mathrm{div}(\rho \vec{V} S) + \frac{2}{3}\rho G \mathrm{tr}(D) I - 2\rho G D = 0, \tag{5}$$

where, D is strain rate tensor, and G is the shear modulus of material.

In the present framework, temperature is obtained from the calculated internal energy from Eq. (3) using the relationship given in Ref. [22]:

$$T(V,e) = T_0(V/V_0)^{\Gamma} + \frac{e - e_C(V)}{C_V}, \tag{6}$$

where C_V is the specific heat at constant volume, T_0 is the reference temperature, i.e., 298 K, V_0 is the reference specific volume, V is the specific volume, and Γ is the Gruneisen coefficient. Detailed description of temperature calculation is provided in previous work [14].

B. Constitutive model for HMX

The material models for HMX used to perform the current 3D mesoscale analysis are based on the work of Menikoff *et al.* [22]. A Birch-Murnaghan equation of state is used for the dilatational response of HMX. The equation of state properties are provided in Menikoff *et al.* [22]. The deviatoric response is obtained by modeling the viscoplastic behavior of HMX under shock loading. Void collapse under shock loading can lead to the melting of HMX; therefore, thermal softening of HMX is modeled using the Kraut-Kennedy relation with model parameters provided in the work of Menikoff *et al.* [22]. Once the temperature exceeds the melting point of HMX, the deviatoric strength terms are set to zero. The specific heat of HMX is known to change significantly with temperature. The variation of specific heat is modeled as a function of temperature as suggested in Ref. [22].

C. Reactive modeling of HMX

The chemical decomposition of HMX is modeled using a three-step mechanism proposed by Tarver *et al.* [20]. A detailed description of the implementation of the three-step model in the current numerical framework is presented in previous work [14]. Here, a brief overview of the reaction model and its implementation is provided.

Chemical decomposition of HMX takes place in three steps involving four different species. The three steps are:

$$\text{Reaction 1 : HMX } (C_4H_8N_8O_8) \rightarrow \text{fragments } (CH_2NNO_2), \tag{7}$$

$$\text{Reaction 2 : fragments } (CH_2NNO_2) \rightarrow \text{intermediate gases } (CH_2O, N_2O, HCN, HNO_2), \tag{8}$$

$$\begin{aligned}\text{Reaction 3 : 2 } \times \text{ intermediate gases } (CH_2O, N_2O, HCN, HNO_2)\\ \rightarrow \text{final gases } (N_2, H_2O, CO_2, CO).\end{aligned} \tag{9}$$

The conversion of solid HMX (species 1, Y_1) to the final gaseous products (species 4, Y_4) completes the decomposition of HMX and causes increase in temperature because of exothermic reactions. The chemical species that are formed after decomposition of HMX are evolved in time by solving the

species conservation equation:

$$\frac{\partial \rho[Y_i]}{\partial t} + \mathrm{div}(\rho \vec{V}[Y_i]) = \dot{Y}_i, \tag{10}$$

where Y_i is the mass fraction of the ith species and $\dot{Y}_i$ is the production rate source term for the ith species.

The numerical stiffness in solving the reactive set of equations is circumvented by using a Strang operator splitting approach [23], where first the advection of species is performed using the flow time step to obtain predicted species values:

$$\frac{\partial \rho[Y_i]^*}{\partial t} + \mathrm{div}(\rho \vec{V}^n[Y_i]^*) = 0. \tag{11}$$

In a second step, the evolution of the species mass fraction due to chemical reactions is calculated:

$$\frac{d\left[Y_i^{n+1}\right]}{dt} = \dot{Y}_i^{*n}. \tag{12}$$

The change in temperature because of the chemical decomposition of HMX is calculated by solving the temperature evolution equation,

$$\rho C_p \dot{T} = \dot{Q}_R + \lambda \Delta T, \tag{13}$$

where, ρ is the density of HMX, C_p is the specific heat of the reaction mixture, T is the temperature, λ is the thermal conductivity of the reaction mixture, Δ is the Laplacian operator, and $\dot{Q}_R$ is the total heat release rate from all the reactions.

The species evolution Eq. (12) and temperature update Eq. (13) are advanced in time using a fifth-order Runge-Kutta Fehlberg [24] method, which uses an internal adaptive time-stepping scheme to deal with the stiffness of the chemical kinetic equations.

D. Numerical algorithms and interfacial conditions

The conservation laws of mass, momentum, and energy [Eqs. (1)–(3)], along with the evolution of deviatoric stresses [Eq. (5)] and reactive set of equations [Eq. (10)] are spatially discretized using a third-order shock capturing ENO scheme [25]. The time integration is performed using a third-order Runge-Kutta scheme. Narrow-band level-set-based tracking [26] is used in the current framework to sharply track the material interfaces. The use of levelset function allows handling of large deformation of interfaces that occurs during void collapse events. The interfacial conditions between the HMX and void are modeled by applying the free surface conditions at the interface using a modified ghost fluid method [27]. It is important to note that void region in HMX is not modeled in the current analysis. Detailed descriptions of the numerical algorithms, level set implementation and interface treatment are provided in previous works [16–19].

III. RESULTS AND DISCUSSION

Three-dimensional reactive void collapse analysis is performed in the present work to understand the void collapse behavior leading to hot-spot formation and reaction initiation. Voids of shapes commonly present in real microstructures of pressed HMX (for example, in Class III and Class V pressed explosives [28]) are idealized to represent the primary geometric features. Idealized shapes, i.e., sphere, cylinder, plate, and ellipsoid (Fig. 1), are employed to capture key attributes of real voids. The rationale for choosing these shapes is as follows: (1) The cylindrical void captures the effect of aspect ratio and orientation with respect to the incident shock and therefore deviates in two respects from the spherical void; (2) The plate-shaped void further alters the aspect ratio along a second (orthogonal) direction relative to the cylindrical void, as can be seen from Figs. 1(b) and 1(c); (3) The ellipsoidal void perturbs the cylindrical shape by changing the curvature along the length of the

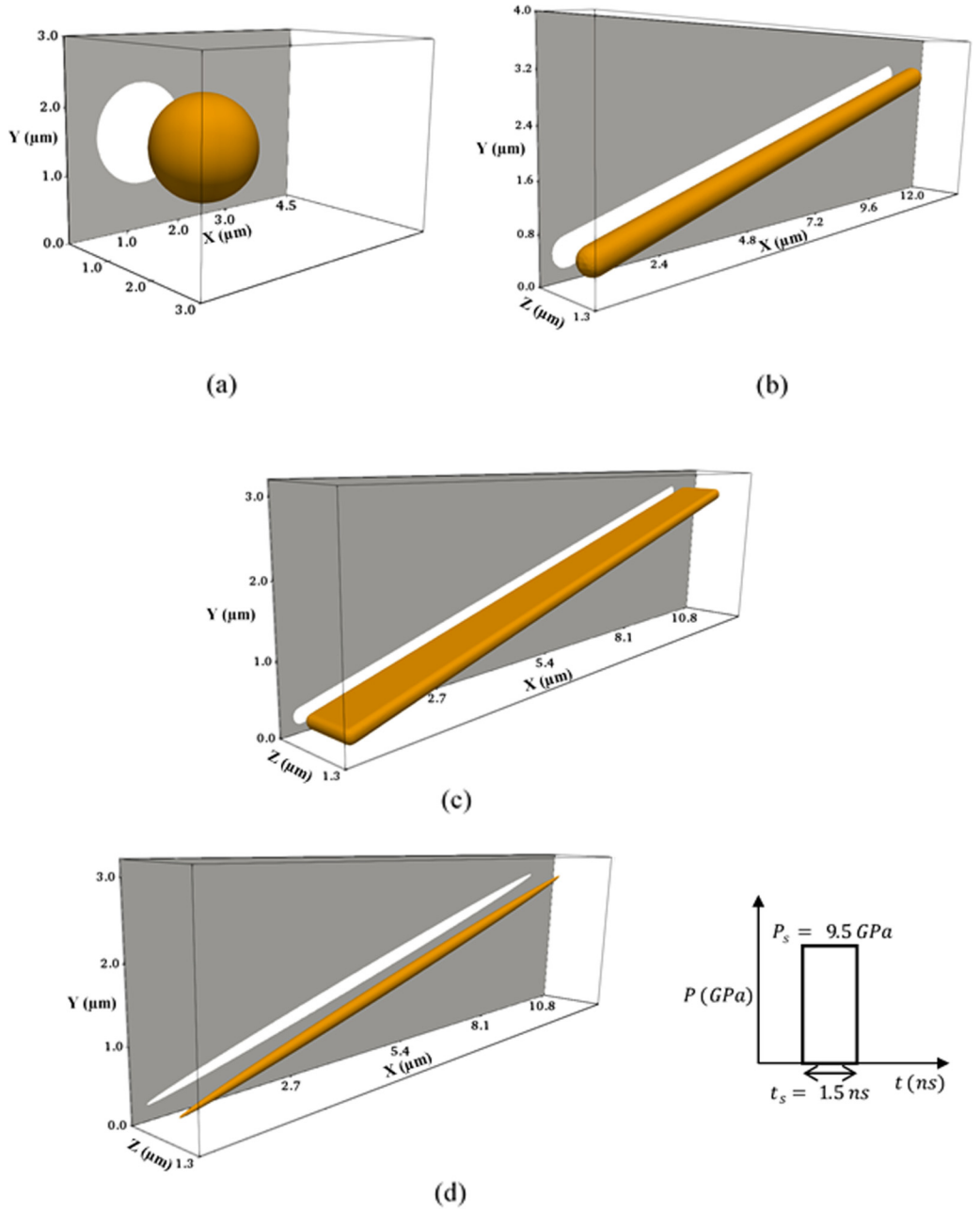

FIG. 1. Numerical set for the 3D reactive void collapse simulations of the four different shape voids, i.e., sphere, cylinder, plate, and ellipsoid. Shock loading in the form of a rectangular pulse of pressure, $P_s = 9.5$ GPa and pulse duration of $t_s = 1.5$ ns is applied from the west face of the domain boundary (along the positive X axis). (a) Spherical void of diameter 1.55 μm in HMX matrix of dimensions 4.5 μm $\times$ 3 μm $\times$ 3 μm, (b) Cylindrical void of diameter 0.5 μm and length 10 μm oriented at an angle of 15° with respect to the positive X-axis in a HMX matrix of dimensions 1.2 μm $\times$ 4 μm $\times$ 1.3 μm, (c) Plate void of dimensions 10 μm $\times$ 0.9064 μm $\times$ 0.2165 μm oriented at an angle of 15° with respect to the positive X-axis in a HMX matrix of dimensions 10.8 μm $\times$ 3.2 μm $\times$ 1.3 μm, and (d) Ellipsoid void with major and minor axes 10 μm and 0.2165 μm oriented at an angle of 15° with respect to the positive X-axis in a HMX matrix of dimensions 10.8 μm $\times$ 3.2 μm $\times$ 1.3 μm.

void, moving from high curvatures at the major axes of the ellipsoid to low curvatures at the minor axes as shown in Fig. 1(d). This last shape therefore represents a rather modest perturbation of the cylindrical shape. One objective of this paper is to examine how alterations in aspects of geometry, represented by the above three types of differences, contribute to changes in void sensitivity. A second objective is to examine what differences, if any, exist between the aforementioned 3D shapes and their 2D counterparts in their response to shock loading.

The sensitivity behavior of the four void shapes is quantified and compared in two different aspects: (a) First, the differently shaped voids (i.e., sphere, cylinder, and plate) are studied for the same loading conditions and the same void volume, so that only differences in the shapes of the voids contribute to differences in hot-spot morphologies and void sensitivity; (b) second, the more subtle effect of void shape on sensitivity is analyzed by comparing the behavior of cylindrical and ellipsoidal voids. For all the simulations, voids are embedded in an otherwise uniform HMX material and are subjected to the same shock loading in the form of a rectangular pulse of strength 9.5 GPa and duration of 1.5 ns from the west face of the domain boundary, as shown in Fig. 1. All other domain boundaries are supplied with zero-gradient boundary conditions. The results obtained from the simulations are presented in three sections. Section III A is focused on understanding the collapse behavior and its implications on the reaction initiation for the four different void shapes mentioned above. In Sec. III B, the sensitivity of the voids is quantified and compared by calculating the reacted HMX mass and hot-spot temperature. Section III C is aimed at evaluating the relative sensitivity of the 3D void shapes relative to their 2D counterparts, with the objective of assessing how assessments of sensitivity calculations and hot-spot formation in 2D compare with the 3D cases.

Detailed verification and validation studies for the void collapse problem in HMX are presented in the previous work [14]. Extensive grid convergence studies for different shock strengths and void geometries, i.e., circular and elongated are shown in previous work as well [8,14]. The grid refinement studies in Ref. [14] have provided guidelines for suitable refinement criteria to obtain grid independent solutions; the guidelines developed from the previous analysis are used to resolve the voids in the current study. Specifics of grid resolution for each void shape are provided below. All simulations presented in the following are performed on DoD HPC machines using 6400 processors.

A. Dynamics of void collapse for various void shapes

Dynamics of void collapse for different void shapes in inert and reactive media has previously been studied using 2D analysis [2,5,8–11,14] or axisymmetric modeling [6,7]. Although the physics of void collapse is well understood in 2D for different void shapes, 3D effects on the collapse behavior and hot-spot formation remain to be examined. In this section, the collapses of spherical and nonspherical voids are analyzed.

1. Collapse behavior of a spherical void

Figure 1(a) shows the computational setup. A spherical void of diameter 1.55 μm is embedded in a HMX domain of size 4.5 μm $\times$ 3 μm $\times$ 3 μm. A uniform grid of size 7.75 nm is used to resolve the spherical void, amounting to 200 grid points across the sphere diameter requiring roughly 85 million grid points in the domain.

Previous 2D void collapse work [8,14], involving circular and elongated voids, indicated the formation of strongly rotational velocity fields at the sites of void collapse. The rotational flows arise due to the generation and instability of baroclinic vortices as the void collapses under the shock load. The collapse and heating of the material lead to density gradients that are misaligned with the pressure gradients accompanying the shock loading, leading to the formation of baroclinic vortices. In 2D, instabilities of the vortex sheets lead to roll-up and formation of concentrated vortical structures, as commonly observed in a wide class of shear layers [29]. The generation of baroclinic vorticity and subsequent instabilities are expected to be more pronounced in 3D, with the additional degree of freedom leading to instabilities in and normal to the plane of the shear layer. To visualize the vorticity field in 3D, standard λ_2 method [30] is used. The eigen values of the tensor, $S^2 + \Omega^2$,

is computed, where S is the rate of deformation tensor and Ω is the spin tensor. The isosurface of negative eigenvalue of the $S^2 + \Omega^2$ tensor, i.e., λ_2, is used to visualize the vortex structures.

Figure 2 shows the time variation of the isosurface of λ_2 colored with the contours of Z component of vorticity, i.e., Ω_z, the deforming spherical void surface under the prescribed shock loading and centerline Z-axis projection showing the contours of the Ω_z in mid XY plane (i.e., along the symmetry axis). Figure 2(a) shows that the early deformation of the void occurs with little vorticity generation. As the collapse progresses, a material jet is formed causing the impact of the front surface of the void onto the downstream surface as shown in Fig. 2(b). This initial jet impact causes the generation of baroclinic vortices as seen from the contour plots of Ω_z in Fig. 2(b). After the void completely collapses, the baroclinic vortices take the form of vortex rings as the curved vortex sheet rolls up, as seen from the isosurface plot of λ_2 in Fig. 2(c). The vortex rings grow and eventually dissociate into multiple rings [Fig. 2(d)]. The resulting multiple vortex rings are advected by the postcollapse blast wave and eventually dissipate.

The collapse of the spherical void leads to the formation of baroclinic vortex rings. It was observed from the 2D analysis of circular voids [14] that the core of the baroclinic vortices coincide with regions of maximum temperature rise and reaction progress. The coincidence of high temperature and chemical reaction is also expected in the case of spherical void. To understand the behavior of spherical void, Fig. 3 shows the time series contour plots of isosurface of λ_2 colored with the contours of final reaction products (Y_4) in the Tarver three-step model [Eq. (9)], the deforming void interface and centerline Z-axis projection showing the contours of temperature. As shown in Fig. 3(a), the shock first starts to deform the front surface of the void and causes the bulk heating of HMX. The formation of the material jet leading to the impact of the front surface of the void to the downstream causes the initial rise in temperature and reaction initiation [Fig. 3(b)]. After the void has completely collapsed, the temperature rise and reaction completion are localized in the core of the baroclinic vortices. This can be seen in Figs. 3(c) and 3(d). The vortex rings eventually disintegrate and dissipate leaving behind a hot spot of high temperature and hot reaction products [Fig. 3(e)]. Note that the dissipation of the vortex rings created at the end of the collapse process result from the combined effects of plastic dissipation, the flow of material from the site of the collapse, advection of the vortex ring, and numerical dissipation at the high-gradient regions as the concentrated hot-spot forms. In summary, the primary features in the collapse of a spherical void are material-jetting followed by baroclinic vortex ring formation and breakdown. The change in the void collapse features with void shape is presented in the following section.

2. Collapse of a high aspect ratio cylindrical void

Two-dimensional simulations [5–8] of void collapse, hot-spot formation, and reaction initiation have shown a strong dependence on void shape, particularly on the aspect ratio and orientation of nonspherical voids [8]. To understand the impact of void shape on sensitivity in 3D, three other void shapes (i.e., cylindrical, plate, and ellipsoid) are analyzed. In all the cases of nonspherical shape, the orientation of voids is maintained at 15° to the incoming shock; 2D simulations [8] show that this orientation lies in the range contributing to the highest sensitivity of elongated voids. Variations of orientation and other complications of shape are not investigated in this work to maintain focus on elucidating the physics of the primary shape features.

First, the collapse of a cylindrical void is presented. Figure 1(b) shows the numerical set up. A cylindrical void of diameter 0.5 μm and length 10 μm oriented at an angle of 15° with the positive X axis is analyzed. The cylindrical void is resolved with 40 points across the cylinder diameter, i.e., 0.5 μm, leading to a grid size of 12.5 nm. The simulation is performed with 86 million grid points. The same visualization strategy as in the case of spherical void collapse is used in the current analysis.

Figure 4 shows the time variation of isosurface of λ_2 colored with the contours of final reaction products, the deforming cylindrical void interface; and centerline Z-axis projection showing the contours of temperature. Figure 4(a) shows that the collapse of the cylindrical void proceeds with the formation of a material jet near the upstream surface of the void. The collapse of the cylindrical

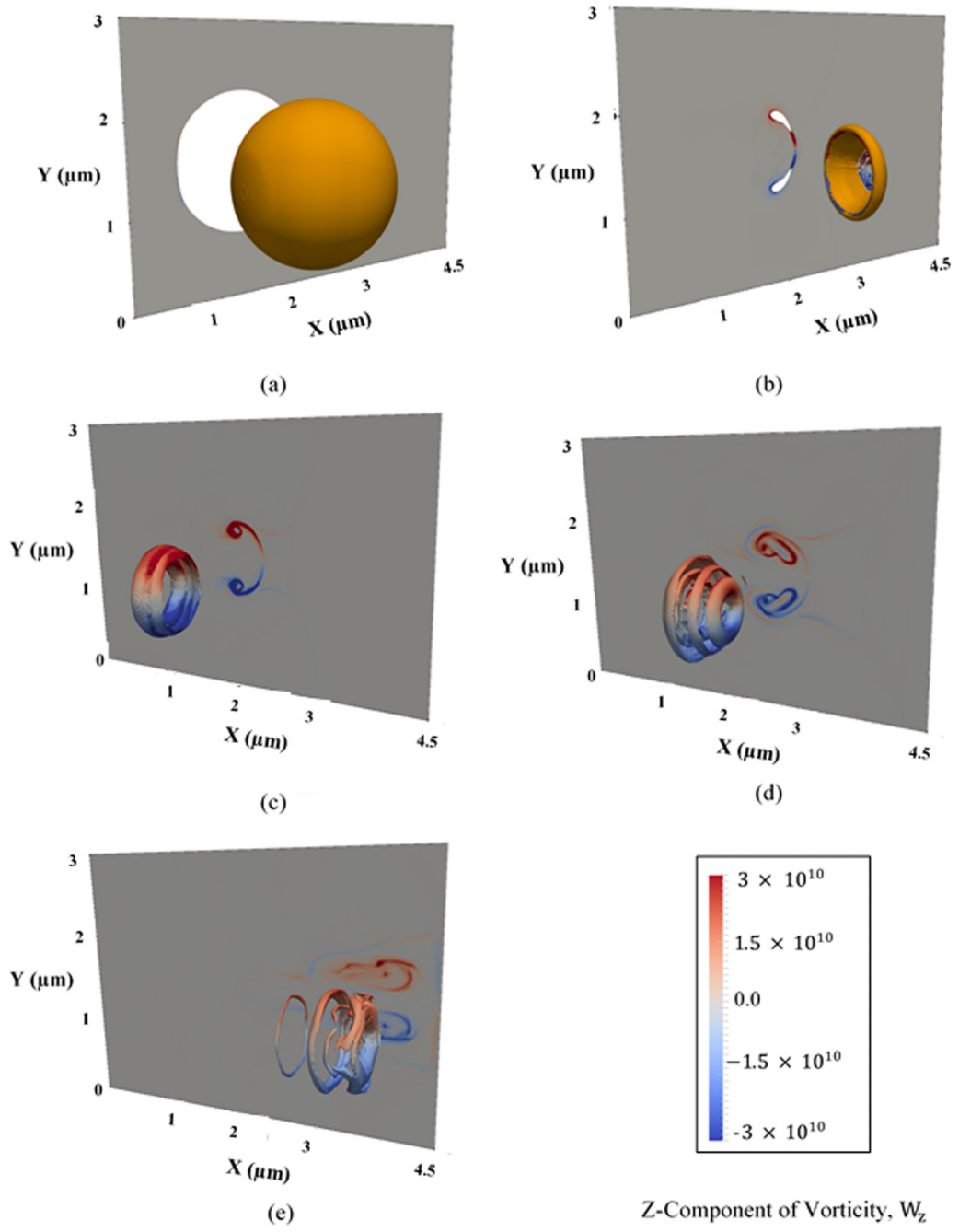

FIG. 2. Contour plots of Z component of vorticity, W_z obtained from the void collapse of spherical void of diameter 1.55 μm under shock load of 9.5 GPa pressure and 1.5 ns pulse duration. The vorticity strength is shown using the isosurface plot of λ_2 colored with the contour of W_z. A 2D projection at the Z-centerline plane is also shown. (a) $t = 0.12$ ns, (b) $t = 0.61$ ns, (c) $t = 0.73$ ns, (d) $t = 0.89$ ns, and (e) $t = 1.4$ ns.

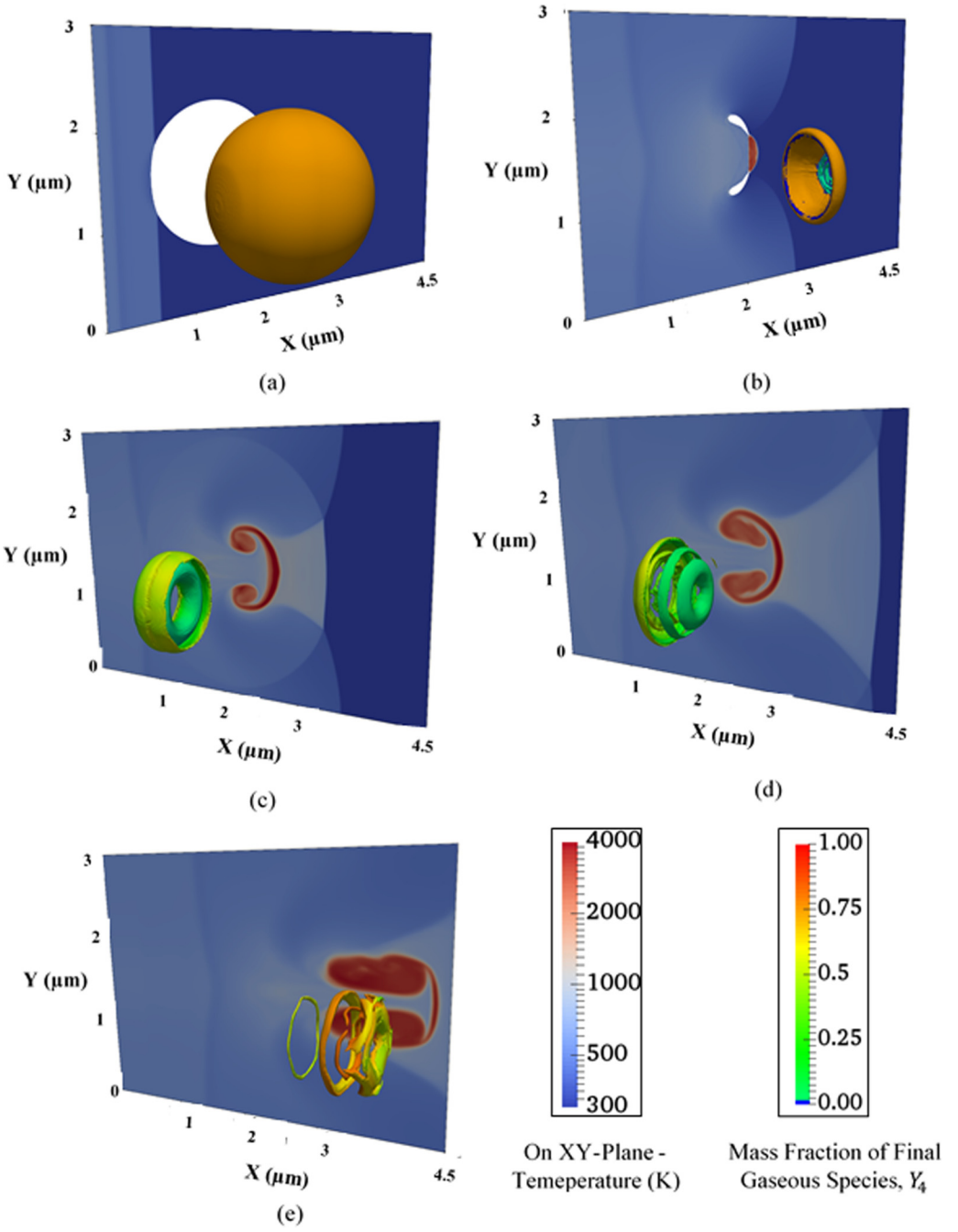

FIG. 3. Contour plots of temperature and mass fraction of final gaseous species, Y_4 at different stages of void collapse of a spherical void of diameter 1.55 μm under shock load of 9.5 GPa pressure and 1.5 ns pulse duration. On the XY plane (centerline Z axis), the contour plot of temperature is shown. The iso-surface of λ_2 colored with the mass fraction of final gaseous species, Y_4, is also shown. (a) $t = 0.12$ ns, (b) $t = 0.61$ ns, (c) $t = 0.73$ ns, (d) $t = 0.89$ ns, and (e) $t = 1.4$ ns.

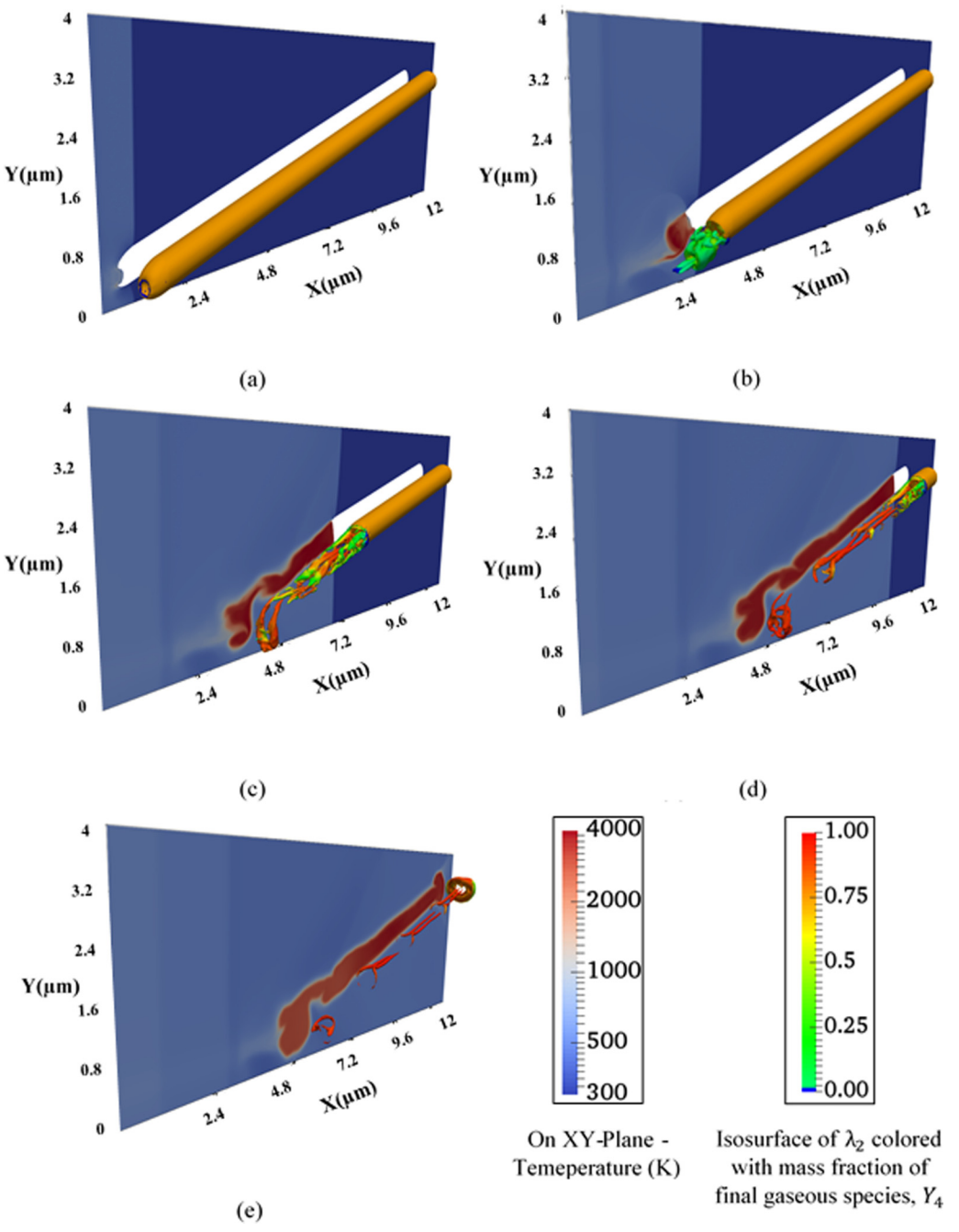

FIG. 4. Contour plots of temperature and mass fraction of final gaseous species, Y_4 at different stages of void collapse of a cylindrical void of diameter 0.5 μm and length 10 μm under shock load of 9.5 GPa pressure and 1.2 ns pulse duration. On the XY plane (centerline Z axis), the contour plot of temperature is shown. The isosurface of λ_2 colored with the mass fraction of final gaseous species, Y_4, is also shown. (a) $t = 0.18$ ns, (b) $t = 0.44$ ns, (c) $t = 1.12$ ns, (d) $t = 1.8$ ns, and (e) $t = 2.49$ ns.

void occurs through repeated pinching events along the length of the void as shown in Fig. 4(b). This is similar to that observed during the collapse of 2D elongated voids [8]. As the collapse progresses, vortices are generated as can be seen from the isosurface of λ_2. Figure 4(c) shows the generation of a horseshoe vortex following the start of the collapse. A succession of collapse events follows, generating more horseshoe-shaped structures. The horseshoe structures interact with each other and are subject to three-dimensional disturbances, which lead to a contorted field of vorticity [Fig. 4(c)]. The regions of high vorticity concentration coincide with the regions of high temperature and maximum reaction progress [Fig. 4(d)]. This observation is similar to what is seen in the case of a spherical void, except for the difference in the shape of the vortex structures. The vorticity field eventually dissipates as in the case of the spherical void leaving behind a hot spot of high temperature and reaction products. The hot spot and reaction zones are localized with regions of high vorticity and micromixing.

3. Collapse behavior of plate void

Next, the collapse behavior of a plate-shaped void is analyzed. Figure 1(c) shows a plate void of dimensions 10 μm $\times$ 0.21 μm $\times$ 0.45 μm oriented at an angle of 15° with positive X axis and embedded in HMX matrix of size 11 μm $\times$ 3.2 μm $\times$ 1.3 μm is analyzed under the applied shock load [Fig. 1(c)]. Grid resolution corresponding to 40 points across the plate thickness (0.21 μm), leading to a grid of size 5.25 nm used to resolve the void. This grid resolution leads to a problem size of 275 million grid points.

Figure 5 shows the time variation of key quantities that evolve during void collapse and hot-spot formation. The collapse of the plate-shaped void starts with formation of a horseshoe vortex as can be seen in Fig. 5(b), similar to the cylindrical void. The progression of the collapse is characterized by a repeated pinching mechanism [Fig. 5(c)]. Due to each successive pinching event, there are a series of vortices formed following the initial horseshoe vortex. The location of these vortices coincides with the regions of maximum temperature rise and reaction completion [Fig. 5(d)]. The interactions of these vortices with each other causes enhanced mixing of reactants, leading to concentration of reaction completion at the locations of intense vorticity. The vortices eventually dissipate and leave an elongated hot spot [Fig. 5(d)]. The collapse behavior of the plate-shaped void appears to be mechanistically similar to the cylindrical void; however, the vorticity concentration is higher in the case of plate-shaped void. This is because, for the same volume of the void, the plate-shaped void presents a larger surface area than the cylindrical void. The slenderness of the plate-shaped void leads to higher concentrations of vorticity, higher levels of instability of the vortex sheet, and therefore more intense micromixing than in the case of the cylindrical void. More quantitative comparisons of the relative strengths of the hot spots because of different void shapes will be presented in Sec. III B.

4. Collapse behavior of ellipsoidal void

The collapse behavior of an ellipsoidal void under shock load is analyzed in this section. Figure 1(d) shows an ellipsoidal void of length 10 μm with equal semimajor and minor axes of 0.2165 μm, oriented at an angle of 15° with respect to the positive X axis. The ellipsoid void is embedded in a HMX matrix of dimensions 11 μm $\times$ 3.2 μm $\times$ 1.3 μm. The ellipsoidal void is resolved with a grid size of 5.25 μm. The grid size is maintained to keep 40 points across the minor axes of the ellipsoid.

The collapse of the ellipsoid is characterized by the generation of series of interconnected horseshoe-shaped vortices as can be seen in Fig. 6(b). The cores of these vortices correspond to the region of maximum temperature rise and reaction initiation [Fig. 6(c)]. This is similar to the case of other voids as well, except that the shape of the vortices in this case is more uniform along the length of the ellipsoid. Pinching of the void surfaces is the dominant collapse mechanism for the ellipsoid void [Fig. 6(d)]. The complete collapse of the void forms an elongated hot spot of high temperature, as can be seen in Fig. 6(e). The primary differences between the ellipsoidal void and the cylindrical void are the sharp ends of the void, i.e., the variation of surface curvature along the void. While this feature may appear to represent a detail in the shape of the void, it does have

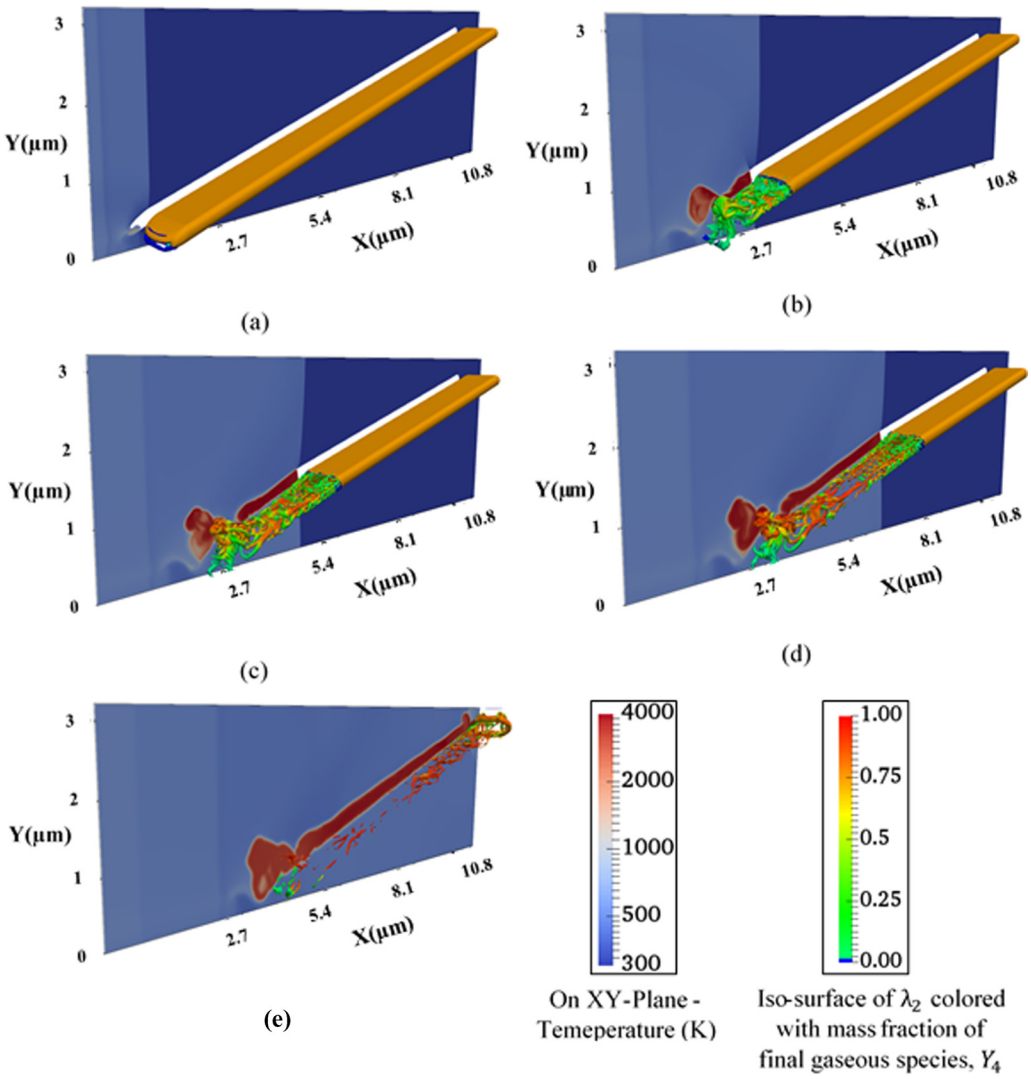

FIG. 5. Contour plots of temperature and mass fraction of final gaseous species, Y_4 at different stages of void collapse of a plate shaped void under shock load of 9.5 GPa pressure and 1.5 ns pulse duration. On the XY plane (centerline Z axis), the contour plot of temperature is shown. The isosurface of λ_2 colored with the mass fraction of final gaseous species, Y_4, is also shown. (a) $t = 0.19$ ns, (b) $t = 0.55$ ns, (c) $t = 0.87$ ns, (d) $t = 1.18$ ns, and (e) $t = 2.26$ ns.

significant impact on the shape and intensity of the hot spot. A quantitative measure of the difference in sensitivity of the ellipsoidal void relative to the rather similar cylindrical void will be presented in Sec. III B.

5. Comparison of collapse behavior of voids

To understand the difference between the vortical structures that arise following complete collapse of the different voids, Fig. 7 shows the λ_2 isosurface colored with the final reaction product for all four voids at a given instant of time during the collapse. For the spherical void, the vorticity field is in the form of concentric rings resulting from the instability of a larger vortex ring structure which

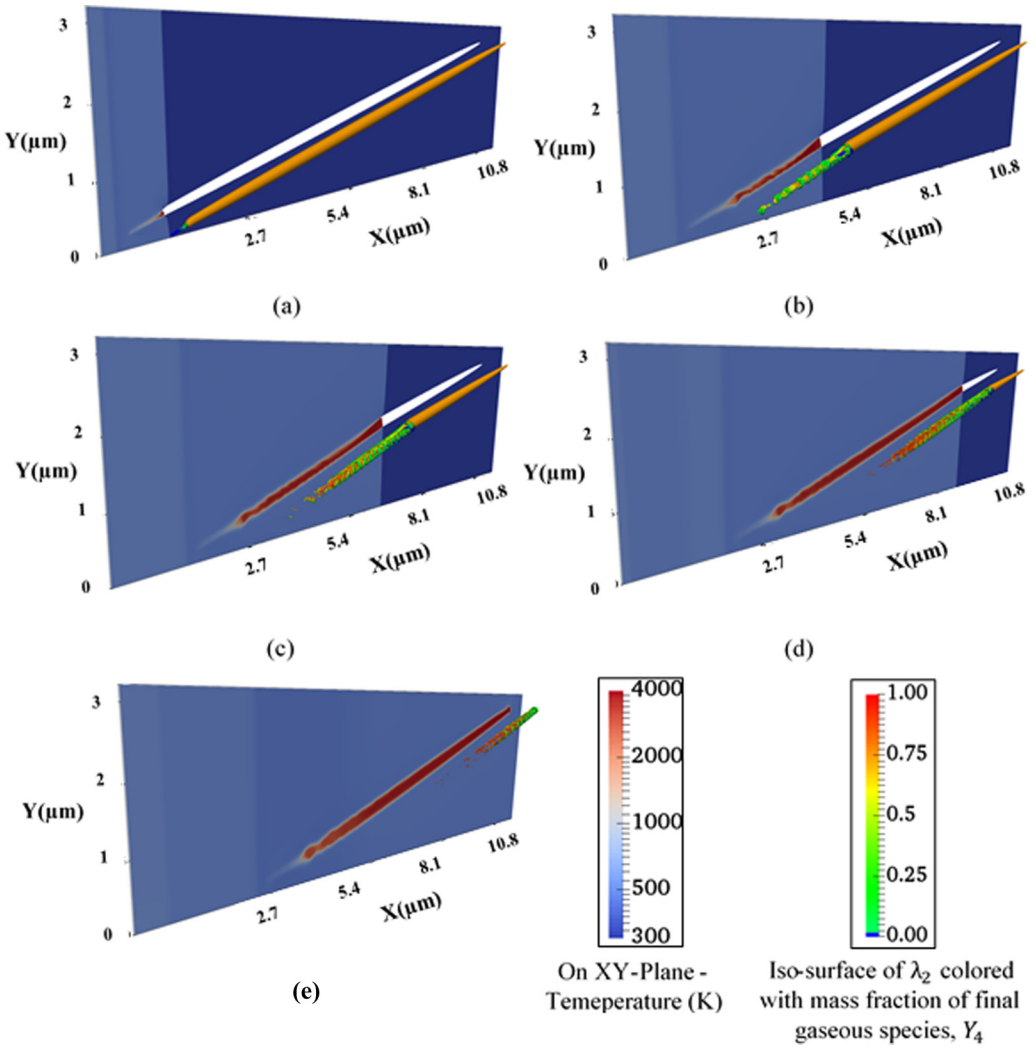

FIG. 6. Contour plots of temperature and mass fraction of final gaseous species, Y_4, at different stages of void collapse of an ellipsoid of major and minor axes 10 μm and 0.2165 μm void under shock load of 9.5 GPa pressure and 1.2 ns pulse duration. On the XY plane (centerline Z axis), the contour plot of temperature is shown. The isosurface of λ_2 colored with the mass fraction of final gaseous species, Y_4, is also shown. (a) $t = 0.2$ ns, (b) $t = 0.59$ ns, (c) $t = 1.06$ ns, (d) $t = 1.54$ ns, and (e) $t = 2.2$ ns.

disintegrated into the observed smaller structures, as shown in Fig. 7(a). Unlike the spherical void, the cylindrical void starts with the formation of a horseshoe vortex followed by a series of contorted vortex structures that interact with each other and are subject to instabilities due to disturbances in the flow field [Fig. 7(b)]. Similar to the cylindrical void, the plate-shaped void also starts with the formation of a horseshoe vortex, although the shape of the horseshoe is more elongated when compared to the cylindrical void, as can be seen in Fig. 7(c). Following the initial horseshoe vortex, there arise a series of complex-shaped vortices that interact with each other to produce smaller-scale structures. One key difference between the vorticity field of cylindrical and plate voids is that the surface area of the isosurface of the vorticity field for the plate void is larger than that for the cylindrical void. This leads to greater mixing and it is expected—and quantitatively verified later in this paper—that higher rates of reaction will result in the case of the plate-shaped void than in the cylindrical case.

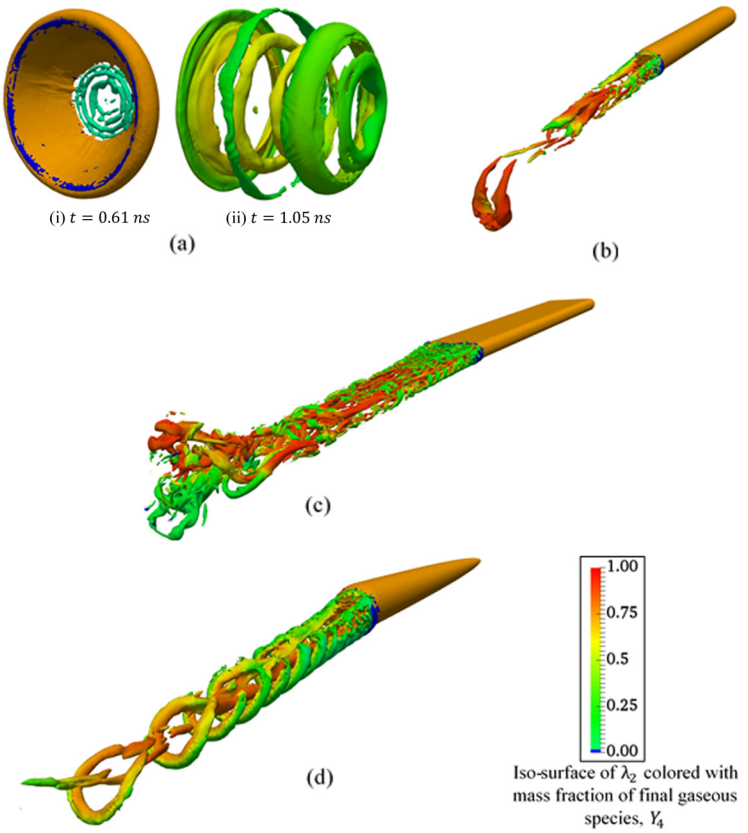

FIG. 7. Void collapse profile of spherical, cylindrical, plate, and ellipsoid void under shock load of 9.5 GPa pressure and 1.5 ns pulse duration. λ_2 profile following the void collapse colored with the mass fraction of final gaseous species, Y_4, is also shown. (a) Collapse profile and λ_2 profile for Spherical Void, (b) Collapse profile and λ_2 profile for Cylindrical Void at $t = 1.8$ ns, (c) Collapse profile and λ_2 profile for Plate Void at $t = 1.18$ ns, and (d) Collapse profile and λ_2 profile for Ellipsoid Void at $t = 1.54$ ns.

Note that the 2D counterparts of both the cylindrical and platelike voids will have an identical shape. Three-dimensional simulations are required to distinguish between the sensitivity of these two types of voids. The vorticity field for the ellipsoidal field is significantly different from the other three void shapes, as can be seen in Fig. 7(d). The collapse of the ellipsoidal void generates a series of horseshoe vortex structures that are interconnected in a braid-like pattern which is commonly observed in vortex wakes behind bluff bodies [29]. The shape of these vortical structures has important implications for the total volume of reacted HMX and the temperature rise in the hot spots.

Apart from the differences between the vorticity fields, the spherical void and nonspherical voids differ significantly in terms of the collapse mechanism. The spherical void collapses because of the formation of a material jet, while the collapse of the other voids involve successive pinching type mechanisms. This is analogous to the 2D case [8,14], involving the circular and elongated voids as pointed out in previous work. The next questions to address are the following: What do 3D simulations reveal regarding the relevance of 2D simulations in understanding hot-spot formation and energetic material sensitivity? And, how do the different void shapes compare in terms of quantitative measures of their sensitivity for a given loading regime? These questions are taken up in the following sections.

B. Quantitative comparison of void sensitivity behavior

Sensitivity of the different voids shapes is quantified using two measures: (1) The total mass of reaction products when the void has completely collapsed, and (2) the average temperature of the hot spot formed after collapse. These two quantities together determine the intensity of the hot spot, in alignment with the critical hot-spot criteria of Tarver *et al.* [20]. The total mass of reaction products is obtained by integrating the mass fraction of final gaseous species (Y_4) over the computational domain, and normalizing with respect to the equivalent mass of HMX in the undeformed void:

$$F = \frac{M_{\text{reacted}}}{M_{\text{void}}} = \frac{\int_V \rho Y_4 dV}{\rho_{\text{HMX}} V_{\text{void}}}. \tag{14}$$

In the above equations, ρ is the density, Y_4 is the mass fraction of the final gaseous products [Eq. (9)], V is volume of the HMX material, ρ_{HMX} is the initial density of unshocked HMX (1900 kg/m^3), V_{void} is the undeformed void volume. M_{void} for the spherical, cylindrical, and plate void is 3.7×10^{-9} μg and M_{void} for the ellipsoid void is 1.82×10^{-9} μg.

The average hot-spot temperature is computed by calculating the volume-average of the temperature field in the hot-spot location. Note that for the shock strength used in the current paper, corresponding to a pressure of 9.5 GPa, the bulk temperature in HMX is around 550 K. In the current analysis, the hot spot is defined as a region of elevated temperature, which is more than the bulk temperature of HMX. The definition of hot spot chosen here aligns with the hot-spot definition provided by Field [1] where the hot spot is defined as the region where temperature is greater than 700 K. Furthermore, for the Tarver-Nichols three-equation HMX decomposition model [20], hot spots with temperatures more than around 700K are required for sustained growth of the reaction front to occur on micro-second time scales. Therefore, in this work the temperature greater than 700 K is used for the hot-spot definition:

$$\text{Average hot-spot temperature,} \quad \bar{T} = \frac{\int_V \rho T_{\text{hot spot}} dV}{\int_V \rho dV}, \tag{15}$$

where $T_{\text{hot spot}}$ is the temperature of the hot-spot region. The volume integral is performed only in the hot-spot location.

The sensitivity of the four void shapes are quantified and compared with respect to the geometrical measures of the voids, such as void volume and surface area, in the next section.

1. Effects of void shapes on sensitivity

To evaluate the effect of void shape, sensitivity of the sphere, cylinder, and plate voids is compared. All three voids have the same void volume of 1.94 μm^3. Therefore, the dependence of sensitivity on the void shapes is analyzed for the same porosity and loading conditions. The time variation of F and $\bar{T}$ for the spherical, cylindrical and plate void is shown in Fig. 8. For the same porosity and loading conditions, the plate-shaped void leads to higher values of F as compared to the cylinder and spherical void as can be seen in Fig. 8(a). A similar trend is observed in the $\bar{T}$ behavior in Fig. 8(b), where the plate void leads to higher temperature rise followed by the cylindrical and spherical voids in that order. Both sensitivity measures indicate that the plate-shaped void is the most sensitive and the spherical void is the least. This observation relates to the vorticity field generated during the collapse of these voids. For the plate-shaped void, the volume occupied by the region of high vorticity is high compared to the cylindrical and spherical void. Since reaction progress is associated with vorticity concentration, the higher volume of vorticity resulting from the collapse of the plate-shaped void corresponds to enhanced micro-mixing, production of F and higher value of $\bar{T}$.

2. Effects of void surface morphology

The difference in the sensitivity behavior of the three voids (i.e., sphere, cylinder, and plate) indicates that void surface morphology has significant influence on sensitivity. To further analyze the importance of void morphology, sensitivity behavior of two relatively similar-shaped voids, i.e.,

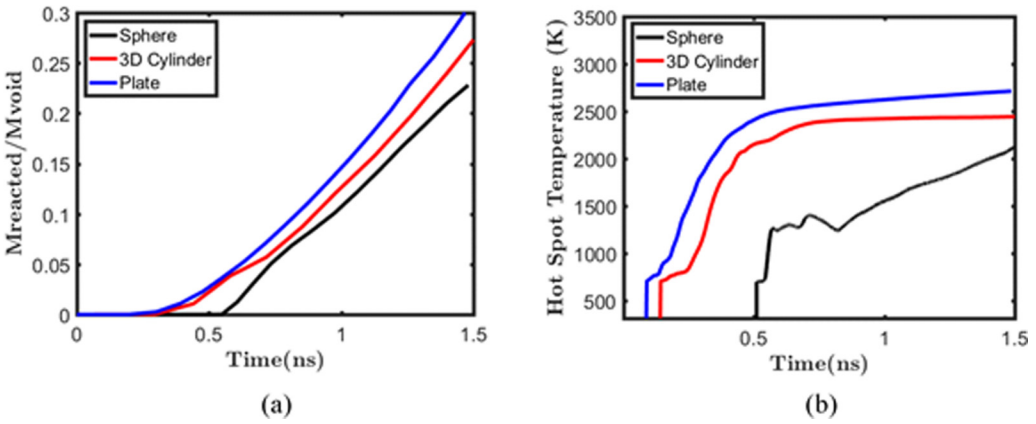

FIG. 8. Comparison between the reacted HMX mass fraction and hot-spot temperature (K) variation with time for the spherical, 3D cylindrical, and plate void of same void volume and under the shock load of 9.5 GPa pressure and 1.5 ns pulse duration. (a) Variation of reacted HMX mass fraction with time and (b) Variation of hot spot temperature (K) with time.

the cylindrical and ellipsoid void of Sec. III A is compared under the same loading conditions. As pointed out earlier, the ellipsoidal void is a modest perturbation of the cylindrical void in regards to changes in curvature along its length; the ellipsoidal void shows high curvature at the tip of the void, which varies to a lower value at the center. Therefore, the comparison between these two voids can show how strongly void sensitivity is dependent on details of the surface morphology.

Figure 9 compares the time variation of the reacted mass of HMX and average hot-spot temperature, $\bar{T}$ for the two voids. The collapse of cylindrical void leads to greater HMX decomposition and reaction product formation, as can be seen in Fig. 9(a). However, the hot-spot temperature rise for both the voids is in the comparable range [Fig. 9(b)]. Although the temperature rise for both the voids is comparable, the high amount of reacted HMX mass for the cylindrical void shows higher sensitivity than the ellipsoid. The difference in the sensitivity of the two voids is related to the vorticity field generated during their collapse. For the ellipsoidal void, the vorticity field is characterized by a

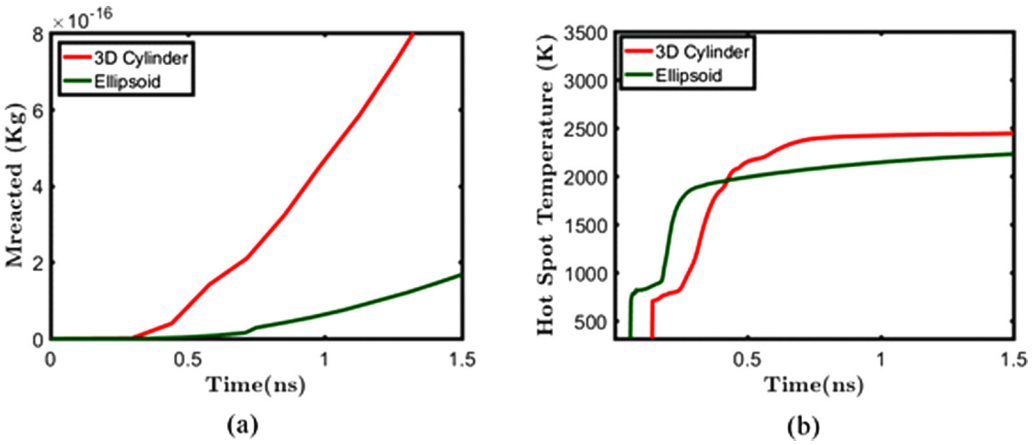

FIG. 9. Comparison between the reacted mass and hot-spot temperature (K) variation with time for a 3D cylindrical and ellipsoid void under the shock load of 9.5 GPa pressure and 1.5 ns pulse duration. (a) Variation of mass reacted with time and (b) Variation of hot spot temperature (K) with time.

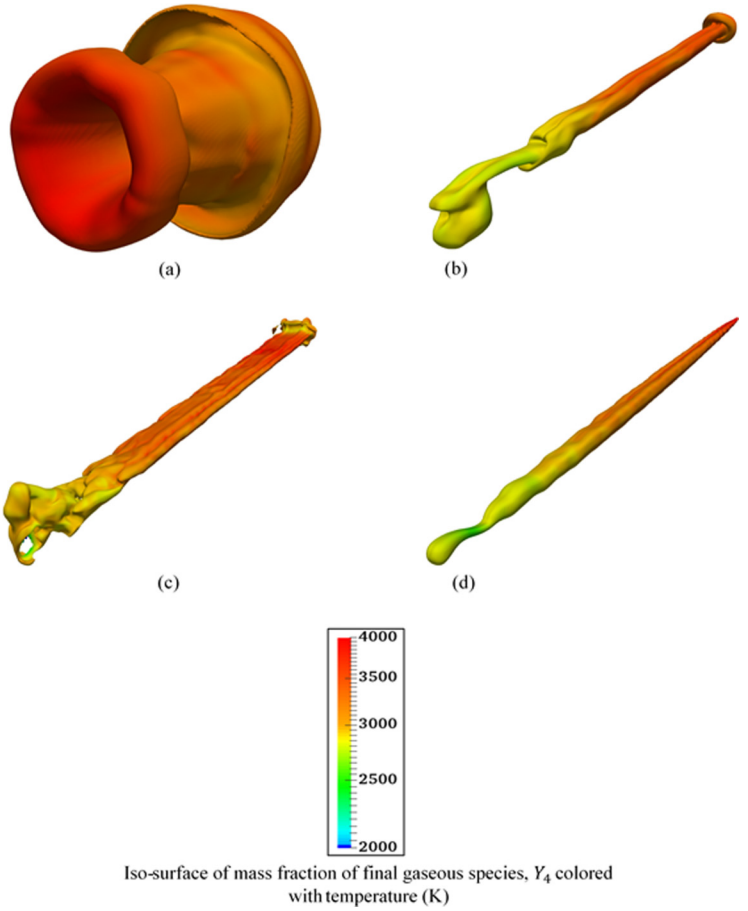

FIG. 10. Isosurface of mass fraction of final gaseous species, Y_4, at value of 0.8 colored with the temperature (K) for spherical, cylindrical, plate, and ellipsoid void after the collapse of the voids. (a) Hot spot shape for spherical void at $t = 1.4$ ns, (b) Hot spot shape for cylindrical void $t = 1.4$ ns, (c) Hot spot shape for plate void at $t = 2.26$ ns, and (d) Hot spot shape for plate void at $t = 2.2$ ns.

series of uniform, tightly formed connected horse shoe vortices, as opposed to the cylindrical void where the vorticity field is more spread out. The spreading of the vorticity field for cylindrical void is a result of complex vortex interactions arising from instabilities of vortices due to disturbances and the induced velocity fields of the interaction vortical structures. The vortex interaction causes intense mixing and reaction, leading to high value of F. The differences in the behavior of cylindrical and ellipsoid void show that even modest differences in void morphology can have important implications for void sensitivity.

3. Effects of void shape on hot-spot formation

To establish the relationship between the void collapse mechanism and hot-spot features for different void shapes, hot-spot information for the four voids is extracted and compared in this section. The hot-spot shape for all the voids is obtained by extracting the isosurface of the final reaction product, Y_4 of value 0.8. The value of 0.8 for Y_4 indicates the regions where 80% HMX is reacted and temperature rise is high. Figure 10 shows the isosurface of Y_4 colored with temperature contours for all the four voids after the voids are collapsed and hot spots are formed. The spherical void forms a mushroom-shaped hot spot as shown in Fig. 10(a). The formation of the mushroom hot

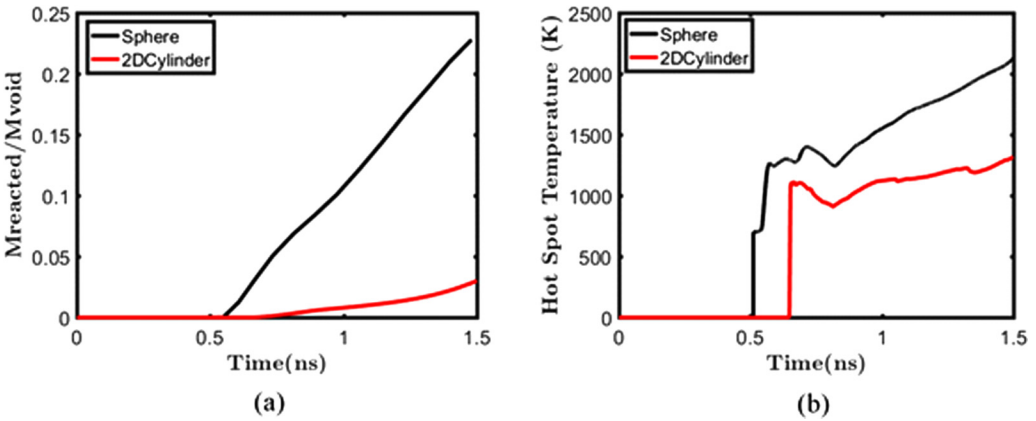

FIG. 11. Comparison between the reacted HMX mass fraction and hot-spot temperature (K) variation with time for spherical void and 2D cylindrical void of same diameter (i.e., 1.55 μm) under the shock load of 9.5 GPa pressure and 1.5 ns pulse duration. (a) Variation of reacted HMX mass fraction with time and (b) Variation of hot spot temperature (K) with time.

spot is related to the material jetting and focusing mechanism of collapse where the jet kinetic energy is localized at the center of the mushroom. The cylindrical void on the other hand forms an elongated hot spot [Fig. 10(b)] generated by the successive pinching mechanism. The plate void generates a long and thin plate shape hot spot with a higher surface area [Fig. 10(c)] than the cylindrical void hot spot. The collapse of the ellipsoid void forms a thin, pointed, and elongated hot spot [Fig. 10(d)]. The hot-spot shape varies with void morphology and is directly related to the initial shape of the void. Therefore, a void with high surface area will form a large hot spot. High surface area of the hot spot increases the reaction growth rates and causes increased sensitivity.

C. Comparison of 2D and 3D analysis

The above 3D void collapse simulations have provided insights into the effect of void shapes on the dynamics of void collapse. However, 3D reactive void collapse analysis is computationally expensive, partly due to rather stringent spatial and temporal resolution requirements [14]. Well-resolved computations in 3D will be intractable for fields of voids that are typical of real microstructures. Currently, the only way to circumvent this problem is to use 2D analysis or axisymmetric modeling. However, axisymmetric modeling is limited to void shapes that have planes of symmetry; this constraint precludes real microstructures. On the other hand, the validity of 2D modeling is not established in the literature. It is particularly important to assess the applicability of 2D analysis for elongated voids because in 3D an elongated void can be present in various shapes, i.e., plate, cylinder, etc. To this end, the comparison of 2D elongated and circular void against their 3D counterparts is performed for a shock loading of 9.5 GPa rectangular pulse with duration of 1.5 ns.

1. Comparison of the collapse of a spherical void with its 2D counterpart

The reaction sensitivity and hot-spot behavior of the spherical void presented in Sec. III A 1 is compared with that of a 2D circular void of the same diameter as the spherical void of 1.55 μm embedded in a HMX domain of size 4.5 μm $\times$ 3 μm.

Figure 11 compares the final gaseous mass fraction F and average hot-spot temperature, $\bar{T}$ for the circular and spherical void. The spherical void collapse leads to greater reaction product F and higher hot-spot temperatures, when compared to the circular void. The spherical void is therefore more sensitive than the circular void. This is because of greater shock focusing in the case of spherical void under three-dimensional loading and collapse than for the 2D case of the circular

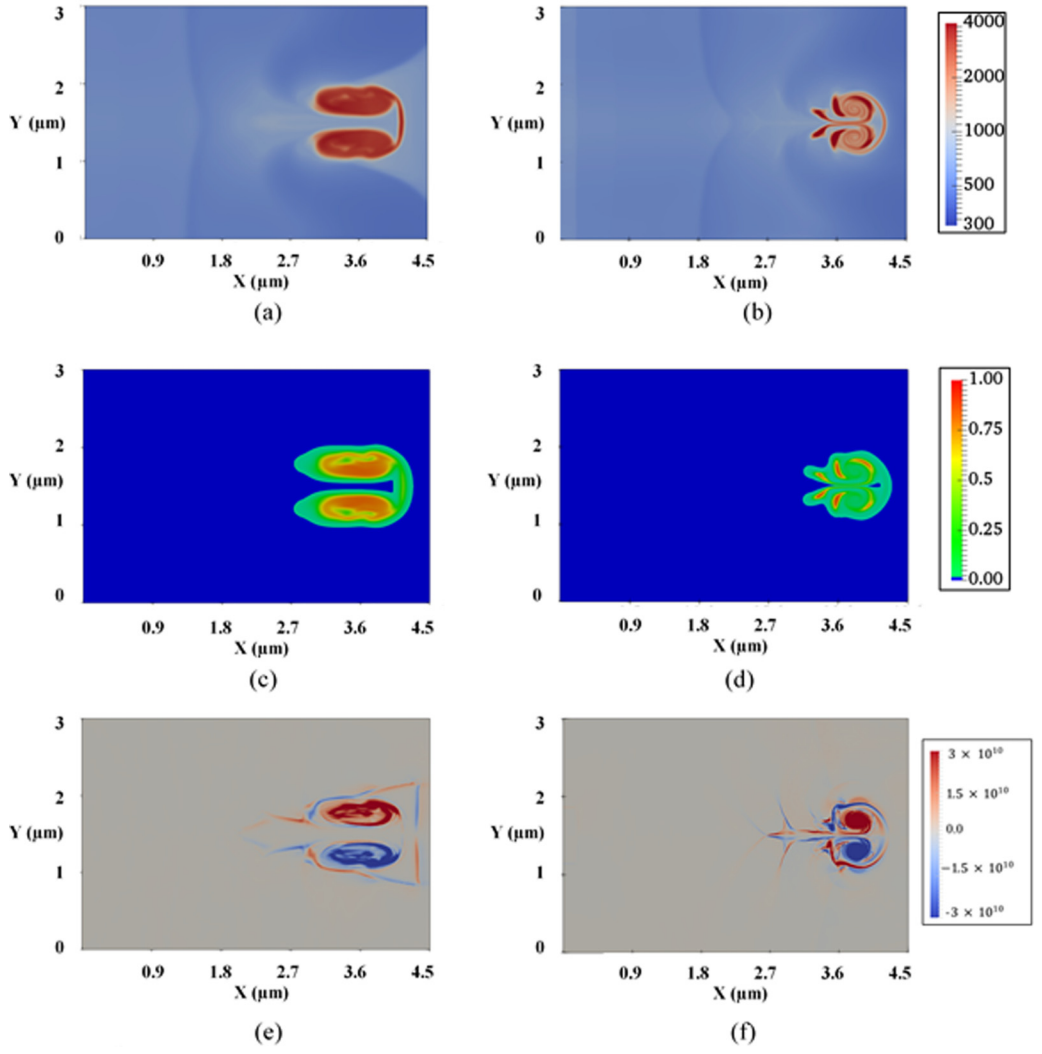

FIG. 12. Comparison between the collapse behavior of spherical void and 2D cylindrical void of same diameter (i.e., 1.55 μm) under the shock load of 9.5 GPa pressure and 1.5 ns pulse duration. (a) Temperature (K) contour on centerline Z-plane at $t = 1.3$ ns from 3D spherical void collapse analysis, (b) Temperature (K) contour from 2D cylindrical void collapse at $t = 1.8$ ns, (c) Mass fraction of final gaseous species, Y_4 contour on centerline Z-plane at $t = 1.3$ ns from 3D spherical void collapse, (d) Mass fraction of final gaseous species, Y_4 contour from 2D cylindrical void collapse at $t = 1.8$ ns , (e) Z-component of vorticity, W_z contour on centerline Z-plane at $t = 1.3$ ns from 3D spherical void collapse, and (f) Z-component of vorticity, W_z contour from 2D cylindrical void collapse at $t = 1.8$ ns.

void. Furthermore, three-dimensionality leads to instabilities, such as the breakdown of the vortex ring into smaller structures that enhance mixing and increase the effective area of heat transfer to the surrounding unburnt HMX. These observations align with previous results [12] where spherical voids were shown to be more sensitive than 2D circular voids.

To gain a deeper understanding of the shape of the hot spot and reaction zones for spherical and circular voids, contour plots of temperature, final gaseous species, Y_4 and Z component of vorticity tensor, Ω_z are presented in Fig. 12. For the spherical void, the contour plots are shown for the central Z plane to directly compare with the results of circular void. Figures 12(a) and 12(b) show that

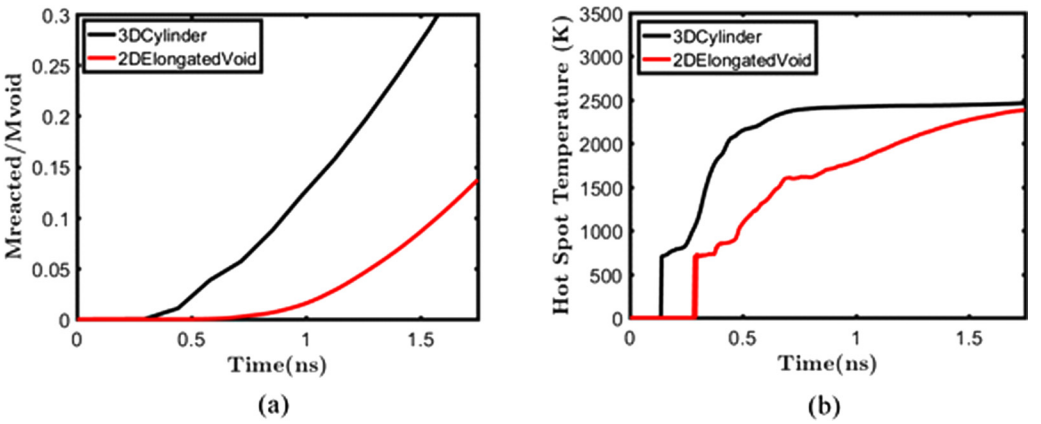

FIG. 13. Comparison between the reacted HMX mass fraction and hot-spot temperature (K) variation with time for 3D cylindrical void and 2D elongated void of same cross-sectional area under the shock load of 9.5 GPa pressure and 1.5 ns pulse duration. (a) Variation of reacted HMX mass fraction with time and (b) Variation of hot spot temperature (K) with time.

the temperature rise after the collapse of the spherical void is higher than the circular void. This observation also applies to the product mass fraction contours and vorticity contours, each of which display stronger magnitudes in the 3D case. The shape of the hot spot in the central plane can be outlined from the temperature contours (by identifying the hot spot as the region with temperatures higher than 700 K); the hot-spot shapes for the 3D and 2D cases are quite different from each other. The spreading of the two side-lobes formed after the initial material-jetting induced collapse of the voids increases the size of the reaction zones in the case of spherical void, resulting in greater temperature rise and mass reacted.

The above results show that the reaction sensitivity of 3D and 2D voids differ significantly and that 2D estimates of hot-spot size and intensity can underpredict the hot-spot-induced sensitivity of porous energetic materials.

2. Comparison of elongated and cylindrical voids in 3D

Elongated voids are prevalent in real microstructures of pressed explosives [28]. The collapse and energy localization behavior of elongated voids was analyzed in previous work [8] using 2D analysis. The limitations of the 2D analysis for elongated voids, are examined in this section in comparison to the behavior of the 3D elongated (cylinder) void of Sec. III A 2. Two-dimensional counterpart of the cylinder-shaped elongated void of thickness 0.5 μm and length 10 μm embedded in the HMX matrix of size 12.5 μm $\times$ 4.2 μm is analyzed. The length and the thickness of the 2D elongated void is maintained, as with the 3D cylindrical void. The shock loading, boundary conditions, and grid resolution are also the same as in the analysis of the 3D cylindrical void in Sec. III A 2.

Figure 13 compares the product mass fraction ratio F and average hot-spot temperature $\bar{T}$ for the 2D and 3D void. The reacted HMX mass fraction, F, is observed to be higher in the 3D case than in 2D [Fig. 13(a)]. The average hot-spot temperature follows a similar trend, as can be seen in Fig. 13(b). To understand the higher sensitivity of a 3D void compared to 2D, Fig. 14 shows the contour plots of temperature, final gaseous products, and Ω_z contours for the 3D and 2D simulations. For the 3D void, the contours are shown at the center Z plane. The contour plots of temperature and the gaseous products show more spreading of the reacted zone for the 3D void as compared to the 2D void. The reason for the spreading of the reaction zone is because of vortex interactions that arise during the collapse of the 3D void, as noted in Sec. III A 2. In the 2D analysis, the vortex interaction

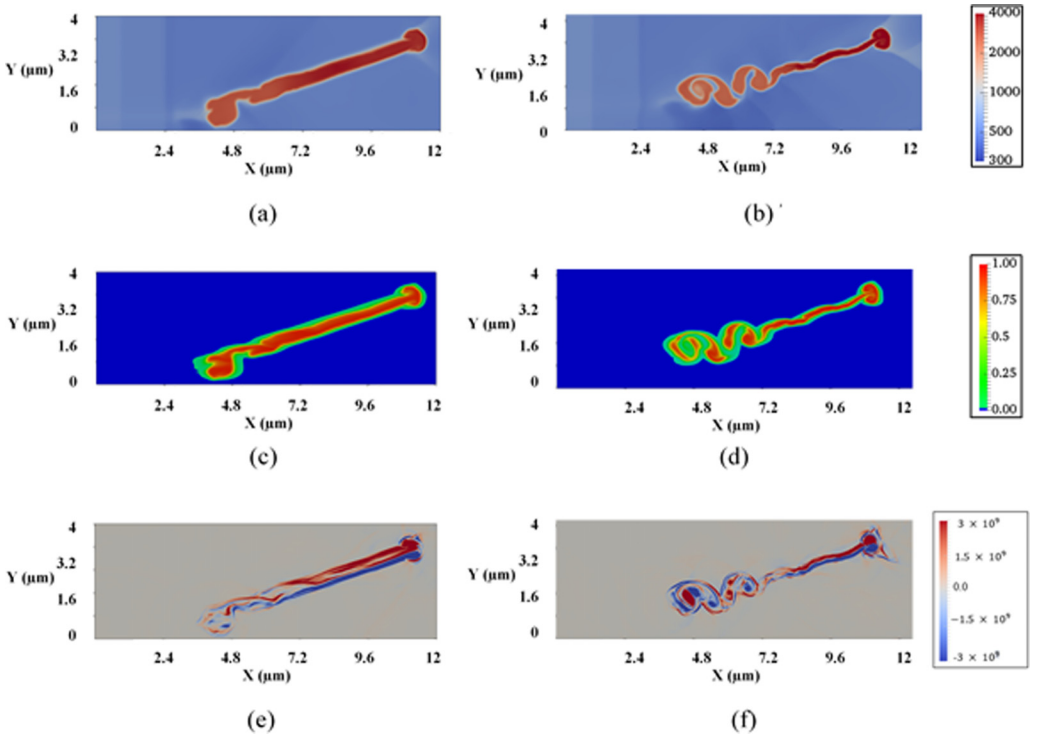

FIG. 14. Comparison between the collapse behavior of a 3D cylindrical void and 2D elongated void of same cross-sectional area under the shock load of 9.5 GPa pressure and 1.5 ns pulse duration. (a) Temperature (K) contour on centerline Z-plane at $t = 2.4$ ns from 3D cylindrical void collapse analysis, (b) Temperature (K) contour from 2D cylindrical void collapse at $t = 2.8$ ns, (c) Mass fraction of final gaseous species, Y_4 contour on centerline Z-plane at $t = 2.4$ ns from 3D cylindrical void collapse analysis, (d) Mass fraction of final gaseous species, Y_4 contour from 2D cylindrical void collapse at $t = 2.8$ ns, (e) Z-component of vorticity, W_z contour on centerline Z-plane at $t = 2.4$ ns from 3D cylindrical void collapse analysis, and (f) Z-component of vorticity, W_z contour from 2D cylindrical void collapse at $t = 2.8$ ns.

is not pronounced [Figs. 14(e) and 14(f)]. The 2D approximation of elongated void to 3D cylindrical underpredicts the hot-spot size and sensitivity as compared to the 3D predictions.

3. Comparison of 2D elongated and plate void in 3D

It was shown above that a 3D cylindrical void is more sensitive than the 2D elongated void. A 2D elongated void can be an approximation for either a 3D cylindrical void or a plate void because both the voids have the same projected geometry in a 2D plane. Therefore, the sensitivity of the plate void of Sec. III A 3 is compared with its 2D counterpart. The length and thickness of the 2D elongated void is the same as the plate void, i.e., 10 μm and 0.21 μm. The void orientation, loading conditions, boundary conditions, and grid resolution is maintained in the plate void collapse analysis (Sec. III A 3).

The final gaseous product mass fraction ratio, F, and the average hot-spot temperature, $\bar{T}$ are compared for the 2D and the 3D void (Fig. 15). Figure 15(a) shows that the reacted mass, F for the 3D void is higher compared to the 2D void. The average hot-spot temperature, $\bar{T}$, for 3D void is higher compared to the 2D predictions [Fig. 15(b)]. The differences in the prediction of F for the 3D plate void and the 2D elongated void are analyzed further by comparing the contour plots of temperature, final gaseous species, and vorticity for the 2D and 3D void (Fig. 16). For the plate

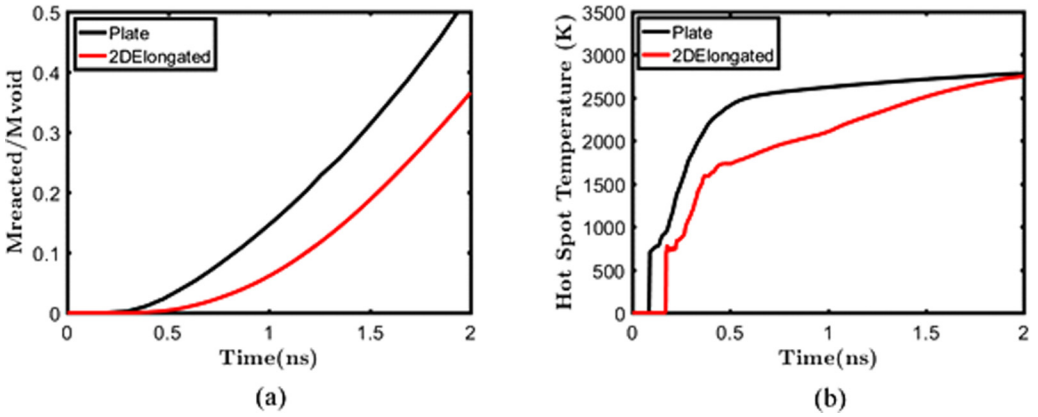

FIG. 15. Comparison between the reacted HMX mass fraction and hot-spot temperature (K) variation with time for 3D plate void and 2D elongated void of same cross-sectional area under the shock load of 9.5 GPa pressure and 1.5 ns pulse duration. (a) Variation of reacted HMX mass fraction with time and (b) Variation of hot spot temperature (K) with time.

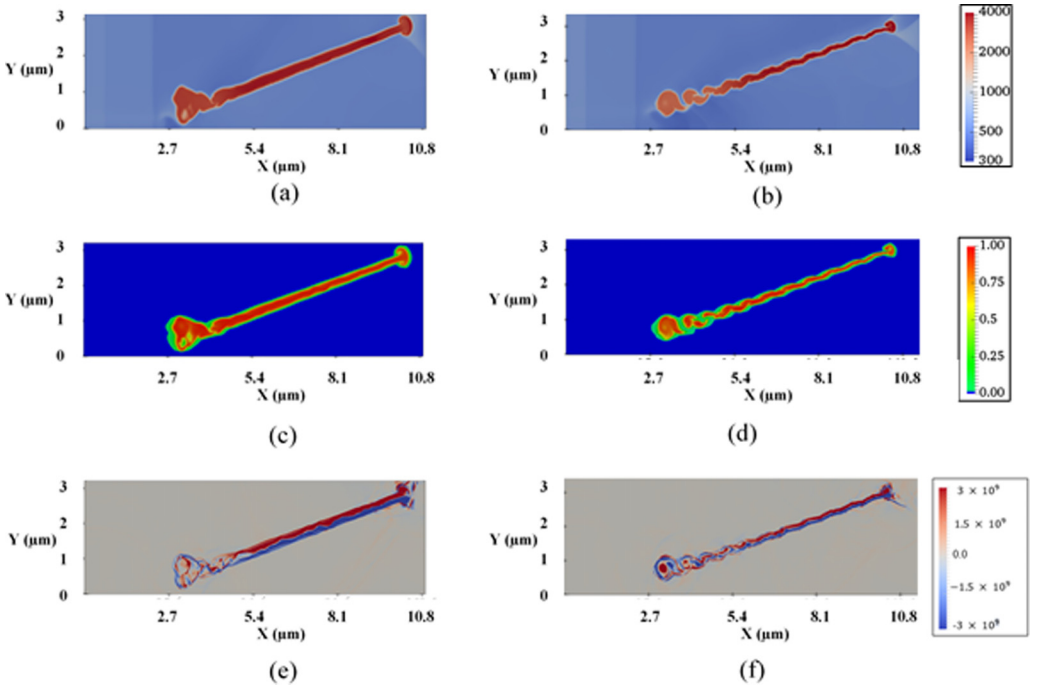

FIG. 16. Comparison between the collapse behavior of a 3D plate void and 2D elongated void of same cross-sectional area under the shock load of 9.5 GPa pressure and 1.5 ns pulse duration. (a) Temperature (K) contour on centerline Z-plane at $t = 2.26$ ns from 3D plate void collapse analysis, (b) Temperature (K) contour from 2D elongated void collapse at $t = 2.44$ ns, (c) Mass fraction of final gaseous species, Y_4 contour on centerline Z-plane at $t = 2.26$ ns from 3D plate void collapse analysis, (d) Mass fraction of final gaseous species, Y_4 contour from 2D elongated void collapse at $t = 2.44$ ns, (e) Z-component of vorticity, W_z contour on centerline Z-plane at $t = 2.26$ ns from 3D plate void collapse analysis, and (f) Z-component of vorticity, W_z contour from 2D elongated void collapse at $t = 2.44$ ns.

void, contour plots at the Z-center plane are shown. The temperature and reaction product contours show that spreading of the reaction zone is greater in the 3D analysis than in 2D [Figs. 16(a) and 16(b)]. Vortical interactions and increased mixing cause the spreading of the reaction zone in 3D [Figs. 16(e) and 16(f)]. Similar to the case of spherical and cylindrical void, the sensitivity of 3D plate void is found to be higher than the 2D counterpart.

IV. CONCLUSIONS

This paper studies the effects of three-dimensionality on void collapse and reaction initiation in HMX. A Cartesian grid based Eulerian framework is used for the high resolution reactive mesoscale simulations of void collapse. A three-step reaction chemistry model is used to calculate the chemical decomposition of solid HMX into gaseous products. The collapse behavior of four different three-dimensional void shapes, i.e., sphere, cylinder, plate, and ellipsoid is analyzed under the shock loading of 9.5 GPa strength and pulse duration of 1.5 ns.

The 3D void collapse simulations provide several insights concerning the collapse behavior of the voids and their sensitivity. First, for all four voids, the collapse generates high-intensity baroclinic vortices. The shapes of the vortical structures change with the shapes of the voids. For the spherical void, vortex rings are formed. For the cylinder- and plate-shaped voids, the collapse starts with the formation of a horseshoe vortex followed by instabilities that create smaller scale vortical structures that interact with each other. Ellipsoidal voids have a region of higher curvature to the incident shock, and the void collapse results in a series of interconnected horseshoe vortices. The location and shape of these vortex structures are important because chemical reactions and heat release are localized in the core of these structures. Therefore, depending on the shape of the voids and the structures generated after collapse, micromixing and concentrations of reaction zones significantly differ depending on the shapes of the 3D voids.

The second insight is that void shape significantly affects the void collapse behavior and its sensitivity. For constant loading and void volume, the plate void has higher sensitivity, followed by cylindrical and then spherical voids. In fact, a modest variation in the void shape from cylinder to ellipsoid undermines the sensitivity of the ellipsoid void under the same loading condition. Voids with higher surface area amount to more HMX burning and increased sensitivity.

Finally, 3D void collapse analysis contributes to higher sensitivity than its 2D counterparts. The reacted HMX mass and hot-spot intensity is significantly higher than in the 2D predictions for all the three voids. The higher sensitivity of voids in 3D is due to the difference in the collapse behavior of voids in 2D and 3D.

The 3D reactive void collapse simulations advance the current understanding of mechanisms of void collapse and its relation to void sensitivity for different void shapes. The sensitivity of voids in 3D is significantly higher for a wide range of void shapes that are commonly present in the microstructures of porous energetic materials. Therefore, 2D assumption should be applied with caution to establish criticality conditions for reaction initiation in energetic materials. Further extensions of the work will analyze the void orientation effects on the sensitivity of non-spherical voids in 3D and quantify the effects of the hot-spot shape on reaction growth rates in HMX. As the 3D simulations are computationally expensive, devising a scaling factor to predict the reaction propagation rates of 3D voids from their 2D counterparts will be considered in the future work.

ACKNOWLEDGMENTS

The authors gratefully acknowledge the financial support from the Air Force Office of Scientific Research (Dynamic Materials Program, program manager: Dr. Martin Schmidt) under Grant No. FA9550-15-1-0332 and EGLIN AFB, AFRL-RWPC (program manager: Dr. Angela Diggs) under the Contract No. FA8651-16-1-0005.

[1] J. E. Field, Hot spot ignition mechanisms for explosives, Acc. Chem. Res. **25**, 489 (1992).
[2] R. Menikoff, *Pore Collapse and Hot Spots in HMX* (Institute of Physics Publishing, London, 2004).
[3] N. Bourne and A. Milne, The temperature of a shock-collapsed cavity, in *Proceedings of the Royal Society of London A: Mathematical, Physical and Engineering Sciences* (The Royal Society, London, 2003).
[4] N. Bourne and J. Field, Bubble collapse and the initiation of explosion, in *Proceedings of the Royal Society of London A: Mathematical, Physical and Engineering Sciences* (The Royal Society, London, 1991).
[5] G. A. Levesque and P. Vitello, The effect of pore morphology on hot spot temperature, Propel. Explos. Pyrotech. **40**, 303 (2015).
[6] A. K. Kapila, D. W. Schwendeman, J. R. Gambino, and W. D. Henshaw, A numerical study of the dynamics of detonation initiated by cavity collapse, Shock Waves **25**, 545 (2015).
[7] H. K. Springer, C. M. Tarver, and S. Bastea, Effects of high shock pressures and pore morphology on hot spot mechanisms in HMX, in *Proceedings of the Conference of the American Physical Society Topical Group on Shock Compression of Condensed Matter*, AIP Conf. Proc. No. 1793 (AIP, Melville, NY, 2017), p. 080002.
[8] N. K. Rai, M. J. Schmidt, and H. Udaykumar, Collapse of elongated voids in porous energetic materials: Effects of void orientation and aspect ratio on initiation, Phys. Rev. Fluids **2**, 043201 (2017).
[9] L. Tran and H. S. Udaykumar, Simulation of Void Collapse in an Energetic Material, Part I: Inert Case, J. Propul. Power **22**, 947 (2006).
[10] L. Tran and H. S. Udaykumar, Simulation of void collapse in an energetic material, Part 2: Reactive case, J. Propul. Power **22**, 959 (2006).
[11] A. Kapahi and H. S. Udaykumar, Dynamics of void collapse in shocked energetic materials: Physics of void–void interactions, Shock Waves **23**, 537 (2013).
[12] A. Kapahi and H. Udaykumar, Three-dimensional simulations of dynamics of void collapse in energetic materials, Shock Waves **25**, 177 (2015).
[13] R. A. Austin, N. R. Barton, J. E. Reaugh, and L. E. Fried, Direct numerical simulation of shear localization and decomposition reactions in shock-loaded HMX crystal, J. Appl. Phys. **117**, 185902 (2015).
[14] N. K. Rai, M. J. Schmidt, and H. Udaykumar, High-resolution simulations of cylindrical void collapse in energetic materials: Effect of primary and secondary collapse on initiation thresholds, Phys. Rev. Fluids **2**, 043202 (2017).
[15] A. B. Swantek and J. M. Austin, Collapse of void arrays under stress wave loading, J. Fluid Mech. **649**, 399 (2010).
[16] S. Sambasivan, A. Kapahi, and H. S. Udaykumar, Simulation of high speed impact, penetration and fragmentation problems on locally refined Cartesian grids, J. Comput. Phys. **235**, 334 (2013).
[17] A. Kapahi, S. Sambasivan, and H. Udaykumar, A three-dimensional sharp interface Cartesian grid method for solving high speed multi-material impact, penetration and fragmentation problems, J. Comput. Phys. **241**, 308 (2013).
[18] N. K. Rai, A. Kapahi, and H. S. Udaykumar, Treatment of contact separation in Eulerian high-speed multimaterial dynamic simulations, Int. J. Numer. Methods Eng. **100**, 793 (2014).
[19] N. K. Rai and H. S. Udaykumar, Mesoscale simulation of reactive pressed energetic materials under shock loading, J. Appl. Phys. **118**, 245905 (2015).
[20] C. M. Tarver, S. K. Chidester, and A. L. Nichols, Critical conditions for impact-and shock-induced hot spots in solid explosives, The J. Phys. Chem. **100**, 5794 (1996).
[21] A. S. Khan and S. Huang, *Continuum Theory of Plasticity* (John Wiley & Sons, New York, 1995).
[22] R. Menikoff and T. D. Sewell, Constituent properties of HMX needed for mesoscale simulations, Combust. Theory Model. **6**, 103 (2002).
[23] G. Strang, On the construction and comparison of difference schemes, SIAM J. Numer. Anal. **5**, 506 (1968).
[24] E. Fehlberg, *Classical Fifth-, Sixth-, Seventh-, and Eighth-Order Runge-Kutta Formulas With Stepsize Control* (National Aeronautics and Space Administration, Washington, DC, 1968).
[25] C.-W. Shu and S. Osher, Efficient implementation of essentially nonoscillatory shock-capturing schemes, II, J. Comput. Phys. **83**, 32 (1989).

[26] S. Osher and J. A. Sethian, Fronts Propagating with Curvature-Dependent Speed—Algorithms Based on Hamilton-Jacobi Formulations, J. Comput. Phys. **79**, 12 (1988).
[27] R. P. Fedkiw, T. Aslam, B. Merriman, and S. Osher, A nonoscillatory Eulerian approach to interfaces in multimaterial flows (the ghost fluid method), J. Comput. Phys. **152**, 457 (1999).
[28] E. J. Welle, C. D. Molek, R. R. Wixom, and P. Samuels, *Microstructural Effects on the Ignition Behavior of HMX* (IOP Publishing, London, 2014).
[29] H. Aref, The development of chaotic advection, Phys. Fluids **14**, 1315 (2002).
[30] M. Jiang, R. Machiraju, and D. Thompson, Detection and visualization of vortices, *The Visualization Handbook* (Elsevier Academic Press, London, 2005), pp. 295–309.